



Periodic lattice microscopic rate equation model for upconversion dynamics and determination of energy transfer microparameters

Boyu Tian ¹, Lin Fu ¹, Yusong Wu ¹, Guanyao Huang¹, and Tairan Fu ^{1,2,*}

¹Key Laboratory for Thermal Science and Power Engineering of Ministry of Education, Beijing Key Laboratory of CO₂ Utilization and Reduction Technology, Department of Energy and Power Engineering, Tsinghua University, Beijing 100084, China

²National Key Laboratory of Ramjet, Tsinghua University, Beijing 100084, China



(Received 30 October 2023; revised 29 April 2024; accepted 11 June 2024; published 2 July 2024)

The upconversion luminescence (UCL) assisted by inter-ion energy transfer has received widespread attention. The inter-ion energy transfer microparameters are the fundamental physical quantities determining the UCL process. However, the experimental exploration of the microparameters has not been reported due to challenges in dynamics models. Here, we report on a universal periodic lattice microscopic rate equation model for upconversion dynamics and determination of the microparameters of energy transfer between ions. In periodic lattices, we propose a processing method for ionic interactions, improving the accuracy of the microscopic model. The random doping of luminescent ions in host lattices often leads to randomness in lattice geometric modeling. Therefore, based on the proposed evaluation criterion for the randomness of lattice modeling, we develop a multiple modeling method for periodic small-scale lattices to replace single modeling of large-scale lattices. This eliminates the influence of randomness in lattice geometric modeling on microscopic model calculations, significantly reducing the computational complexity of the microscopic model (reducing computational time by three orders of magnitude) while ensuring model accuracy. Accurate correlation is actualized from micro-ion interactions to macroluminescence. Using this microscopic model and combined with experimental data on luminescence decay curves at multiple energy levels and ion doping concentrations, 19 inter-ion energy transfer microparameters of Er³⁺ ions in β -NaYF₄:Er³⁺ are determined.

DOI: [10.1103/PhysRevB.110.045105](https://doi.org/10.1103/PhysRevB.110.045105)

I. INTRODUCTION

Upconversion luminescence (UCL) is a nonlinear optical process that converts the excitation of low-energy photons into the emission of high-energy photons [1–4]. Lanthanide ion-doped UCL materials have been widely used in biomedicine [5–11], optical imaging [3,5,12–18], security and anticounterfeiting [13,19–21], and data storage [12,13,21,22]. Inter-ion energy transfer is the driving force for continuous UCL [17,20,23,24], and the inter-ion energy transfer microparameters are the fundamental physical quantities which are of great significance for quantitatively predicting the UCL phenomenon and revealing the upconversion mechanisms.

However, due to the inherent limitations of existing UCL dynamic models in application, accurately determining the inter-ion energy transfer microparameters based on the models has always been a challenge. The macroscopic rate equation model is a classic statistical model characterizing UCL [5,17,18,24–28]. However, it is limited by assumptions of infinitely fast energy migration between ions and uniform ion distribution [29]. Inokuti and Hirayama [30], Yokota and Tanimoto [31], Martin *et al.* [32], and Zusman [33] introduced dynamics models with analytical solutions for luminescence systems with simple energy levels, but they cannot be used for the nonlinear upconversion systems [34]. The microscopic rate equation model [4,35,36] and the Monte Carlo method

[13,37–39] can directly simulate the ion interactions in upconversion systems. However, the computational complexity of large-scale ion clusters involving multiple energy levels, physical processes, and time scales is very large, and there are great difficulties in accurate calculations.

In this paper, we propose a universal and precise UCL dynamics microscopic model with high computational efficiency and accuracy, which can be used to determine the microparameters of energy transfer between ions. In traditional microscopic models, to avoid a significant increase in computational complexity, small-scale lattice geometric modeling is usually used. However, we found that this will lead to the neglect of lattice edge and size effects, resulting in substantial errors. By comprehensively modeling the energy transfer processes in periodic lattices, we propose a processing method for ionic interactions in periodic lattices to improve the accuracy of the microscopic model. Based on the proposed evaluation criterion for the randomness of lattice geometric modeling, we establish a multiple modeling method for periodic small-scale lattices to eliminate the influence of randomness in lattice modeling on microscopic model calculations. This reduces the computational complexity of the microscopic model while ensuring its accuracy. Finally, utilizing our microscopic model, the energy transfer microparameters between Er³⁺ ions in the β -NaYF₄:Er³⁺ six-level system are determined by measuring the luminescence decay curves at different energy levels and ion doping concentrations and solving the inverse problem of this microscopic model. From physical and mathematical perspectives,

*Contact author: trfu@mail.tsinghua.edu.cn

accurate correlation is actualized from micro-ion interactions to macroluminescence. In this paper, we provide important theoretical and computational tools for the regulation and design of upconversion systems and promote the innovative applications of UCL.

II. LIMITATIONS OF TRADITIONAL MICROSCOPIC RATE EQUATION MODEL

The key to the microscopic rate equation model is to model the interactions among many ions. By considering the ionic interactions within the modeled lattice, the traditional microscopic rate equation model (TMI) [4,35,36] can be used for the microscopic characterization of inter-ion energy transfer in upconversion systems. Taking the β -NaYF₄:Er³⁺ system as an example, the modeling steps of TMI are as follows. First, the lattice geometric modeling is performed to obtain the spatial coordinates \mathbf{r}_{e_i} ($i = 1, 2, \dots, n$) of Er³⁺ ions e_i ($i = 1, 2, \dots, n$) in the modeled lattice E . The distance between ion e_i and e_j is $r_{e_i, e_j} = |\mathbf{r}_{e_j} - \mathbf{r}_{e_i}|$. Secondly, considering the ionic interactions within lattice E , the rate of the change of the population probability $P_k^{e_i}$ of ion e_i at energy level k over time t is represented as

$$\begin{aligned} \frac{dP_k^{e_i}}{dt} = & - \sum_{k^*} (w_{a, kk^*} + w_{r, kk^*} + w_{nr, kk^*}) P_k^{e_i} \\ & + \sum_{k^*} (w_{a, k^*k} + w_{r, k^*k} + w_{nr, k^*k}) P_{k^*}^{e_i} \\ & - \sum_m \left[\sum_s \left(C_{km}^{(s)} \sum_{j \neq i} d_{e_i, e_j}^{(s)} P_m^{e_j} \right) P_k^{e_i} \right] \\ & + \sum_{k^*m^*} \left[\sum_s \left(C_{k^*m^*}^{(s)} \sum_{j \neq i} d_{e_i, e_j}^{(s)} P_{m^*}^{e_j} \right) P_{k^*}^{e_i} \right], \quad (1) \end{aligned}$$

where w_{a, kk^*} , w_{r, kk^*} , and w_{nr, kk^*} represent the stimulated absorption rate, radiative relaxation rate, and multiphonon relaxation rate for the single-ion process $k \rightarrow k^*$, respectively; $C_{km}^{(s)}$ is the energy transfer microparameter for the energy transfer process $k + m \rightarrow k^* + m^*$; $s = 6, 8, 10$ represent dipole-dipole, dipole-quadrupole, and quadrupole-quadrupole interactions, respectively; and $d_{e_i, e_j}^{(s)}$ is the distance coefficient between ions e_i and e_j :

$$d_{e_i, e_j}^{(s)} = \begin{cases} 0, & i = j, \\ r_{e_i, e_j}^{-s}, & i \neq j. \end{cases} \quad (2)$$

The rate of the change of the population probability matrix $\mathbf{p}_k(E)$ for all Er³⁺ ions in lattice E at energy level k over time t is represented as

$$\begin{aligned} \frac{d\mathbf{p}_k(E)}{dt} = & - \sum_{k^*} (w_{a, kk^*} + w_{r, kk^*} + w_{nr, kk^*}) \mathbf{p}_k(E) \\ & + \sum_{k^*} (w_{a, k^*k} + w_{r, k^*k} + w_{nr, k^*k}) \mathbf{p}_{k^*}(E) \end{aligned}$$

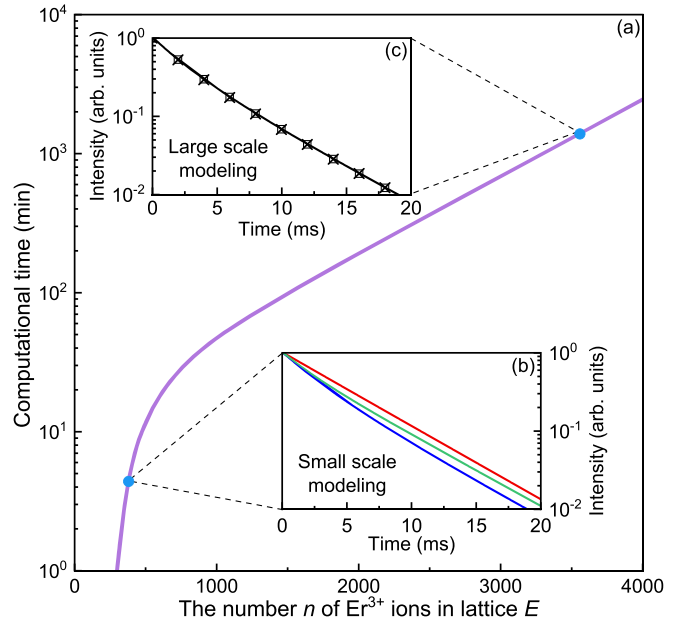


FIG. 1. (a) The relationship between the time required to solve the traditional microscopic rate equations and the number n of Er³⁺ ions in lattice E . The CPU is Intel Core i7-12700H. (b) At a small lattice modeling scale, the luminescence decay curves obtained by solving the traditional microscopic rate equations based on the lattice geometric modeling at the same scale. The red, green, and blue lines represent the luminescence decay curves obtained through lattice rate equations for the first, second, and third times, respectively. (c) At a large lattice modeling scale, the luminescence decay curves obtained by solving the traditional microscopic rate equations based on the lattice geometric modeling at the same scale. The solid line, squares, and crosses represent the luminescence decay curves obtained through lattice geometric modeling at the same scale and solving the microscopic rate equations for the first, second, and third times, respectively. In the subgraphs (b) and (c), the laser excitation occurs within the time interval of $-15 \text{ ms} \leq t \leq 0 \text{ ms}$ (not shown in the figure).

$$\begin{aligned} & - \sum_m \left[\sum_s (C_{km}^{(s)} \mathbf{D}_{E-E}^{(s)}) \mathbf{p}_m(E) * \mathbf{p}_k(E) \right] \\ & + \sum_{k^*m^*} \left[\sum_s (C_{k^*m^*}^{(s)} \mathbf{D}_{E-E}^{(s)}) \mathbf{p}_{m^*}(E) * \mathbf{p}_{k^*}(E) \right], \quad (3) \end{aligned}$$

where $\mathbf{p}_k(E) = [P_k^{e_1} \ P_k^{e_2} \ \dots \ P_k^{e_n}]^T$; $*$ denotes the Hadamard product of the matrices; and $\mathbf{D}_{E-E}^{(s)}$ is the distance coefficient matrix between Er³⁺ ions in lattice E , $\mathbf{D}_{E-E}^{(s)} = [d_{e_i, e_j}^{(s)}]$. Equation (3) is the complete form of TMI.

The relationship between the time required to solve the traditional microscopic rate equations and the number n of Er³⁺ ions in lattice E is shown in Fig. 1(a). As the number n of Er³⁺ ions in lattice E increases, the computational time significantly increases nonlinearly. To ensure the computational feasibility of solving the forward and inverse problems of the model, it is necessary to reduce the scale n of lattice geometric modeling, which is a conventional strategy. However, using small-scale lattice geometric modeling in TMI has the following drawbacks:

(1) *The randomness of lattice geometric modeling is relatively large.* In the lattice geometric modeling of TMI, the random doping of Er^{3+} ions in the $\beta\text{-NaYF}_4$ lattice leads to randomness in lattice geometric modeling. If the scale of lattice geometric modeling is not large enough, the modeling randomness will not be small. This leads to the modeled lattice E not accurately representing the actual spatial distribution of Er^{3+} ions. Under the influence of randomness in lattice modeling, there is a significant deviation in the calculation results of the microscopic rate equations [Fig. 1(b)]. To avoid this phenomenon, it is necessary to increase the scale of lattice modeling [Fig. 1(c)]. However, when n increases from 300 to 3300, the computational time increases by three orders of magnitude.

(2) *The bias caused by ignoring the lattice edge and size effects is significant.* (i) Analysis of the lattice edge effect: Figure 2(a) qualitatively illustrates the distribution of Er^{3+} ions in space. The Er^{3+} ion numbered 0 is located at the edge of lattice E . In TMI, only the ionic interactions in lattice E are considered. Although the Er^{3+} ions numbered 5, 6, 7, and 8 are located very close to the Er^{3+} ion numbered 0, their interactions with the Er^{3+} ion numbered 0 are neglected due to their location outside lattice E (i.e., neglecting the lattice edge effect). When the scale of lattice modeling is small, the ratio n_{edge}/n is large (n_{edge} is the number of Er^{3+} ions located at the edge of lattice E), and the deviation caused by neglecting the lattice edge effect is significant. (ii) Analysis of lattice size effect: As shown in Fig. 2(b), there is a correlation between the number n_{eff} of ions (blue) interacting with the investigated ion (red) and the lattice modeling scale n , $n_{\text{eff}} = n - 1$. When the lattice modeling scale n is small, n_{eff} is also small, leading to a significant underestimation of the ionic interactions (i.e., the deviation caused by neglecting the lattice size effect is significant). (iii) The impact of ignoring the lattice edge and size effects: The periodic lattice microscopic rate equation model (PMI, see Sec. III) proposed in this paper considers both the lattice edge effect [Fig. 2(c)] and the lattice size effect [Fig. 2(d)]. Using TMI and PMI, the macroscopic energy-transfer rates $W_{\text{et},22,n-\text{es}}^{(6)}$ and $W_{\text{et},22,\text{es}}^{(6)}$ corresponding to the two models for the ${}^4I_{13/2} + {}^4I_{13/2} \rightarrow {}^4I_{15/2} + {}^4I_{9/2}$ process are respectively calculated [Fig. 2(e)] (see Sec. A in the Supplemental Material [40] for details of calculations). When lattice E contains 12, 12, and 10 $\beta\text{-NaYF}_4$ unit cells in the x , y , and z directions, neglecting lattice edge and size effects results in an underestimation of approximately 12% in the macroscopic energy-transfer rate.

Therefore, under the constraints of factors such as computational time, randomness of lattice geometric modeling, lattice edge effect, and lattice size effect, TMI struggles to describe the microscopic interactions between ions efficiently and accurately.

III. PERIODIC LATTICE MICROSCOPIC RATE EQUATION MODEL

To overcome the shortcomings of TMI, we propose the periodic lattice microscopic rate equation model (PMI), which has high computational efficiency and wide applicability. This proposed model considers the lattice edge and size effects, greatly improving computational accuracy. We establish an evaluation criterion for the randomness of lattice modeling. Based on this, a multiple modeling method for periodic small-scale lattices is proposed to replace the single modeling of large-scale lattices. This eliminates the influence of randomness in lattice modeling on microscopic model calculations. On the premise of ensuring model accuracy, the computational time can be significantly reduced. Taking the $\beta\text{-NaYF}_4:\text{Er}^{3+}$ six-level system as an example, we will introduce this microscopic model work in this section.

A. Processing method for ionic interactions in periodic lattices

We take $\beta\text{-NaYF}_4:\text{Er}^{3+}$ microcrystalline particle U with a size of 1–2 μm (Fig. 3) as an example to illustrate the processing method for ionic interactions in periodic lattices. First, the lattice geometric modeling is performed to obtain the spatial coordinates \mathbf{r}_{e_i} ($i = 1, 2, \dots, n$) of Er^{3+} ions e_i ($i = 1, 2, \dots, n$) in the modeled lattice E (see Sec. III B and Sec. B in the Supplemental Material [40] for lattice modeling methods). Secondly, periodic lattice modeling is performed by translating lattice E along the vectors \mathbf{M}_g ($g = 1, 2, \dots$) to form a series of periodic lattices V_g . Particle U can be seen as composed of lattice E and its periodically translational lattices V_g . The spatial coordinate of the ion v_{g_i} in V_g is $\mathbf{r}_{v_{g_i}} = \mathbf{r}_{e_i} + \mathbf{M}_g$, and the distance between ions e_i and v_{g_j} is $r_{e_i, v_{g_j}} = |\mathbf{r}_{e_i} - \mathbf{r}_{e_j} + \mathbf{M}_g|$.

Considering the interactions between the Er^{3+} ion e_i in lattice E and Er^{3+} ions (e_j, v_{g_j}) in all lattices of the microcrystalline particle U , the rate of the change of the population probability $P_k^{e_i}$ of ion e_i at energy level k over time t is represented as

$$\begin{aligned} \frac{dP_k^{e_i}}{dt} = & - \sum_{k^*} (w_{a,kk^*} + w_{r,kk^*} + w_{nr,kk^*}) P_k^{e_i} + \sum_{k^*} (w_{a,k^*k} + w_{r,k^*k} + w_{nr,k^*k}) P_{k^*}^{e_i} \\ & - \sum_m \left[\sum_s \left(C_{km}^{(s)} \sum_{j \neq i} d_{e_i, e_j}^{(s)} P_m^{e_j} \right) P_k^{e_i} \right] + \sum_{k^* m^*} \left[\sum_s \left(C_{k^* m^*}^{(s)} \sum_{j \neq i} d_{e_i, e_j}^{(s)} P_{m^*}^{e_j} \right) P_{k^*}^{e_i} \right] \\ & - \sum_m \left\{ \sum_s \left[C_{km}^{(s)} \sum_g \left(\sum_j d_{e_i, v_{g_j}}^{(s)} P_m^{v_{g_j}} \right) \right] P_k^{e_i} \right\} + \sum_{k^* m^*} \left\{ \sum_s \left[C_{k^* m^*}^{(s)} \sum_g \left(\sum_j d_{e_i, v_{g_j}}^{(s)} P_{m^*}^{v_{g_j}} \right) \right] P_{k^*}^{e_i} \right\}, \end{aligned} \quad (4)$$

where $d_{e_i, e_j}^{(s)}$ and $d_{e_i, v_{gj}}^{(s)}$ are the distance coefficients between ions e_i and e_j and between ions e_i and v_{gj} , respectively, and $d_{e_i, v_{gj}}^{(s)} = r_{e_i, v_{gj}}^{-s}$. The fifth and sixth items on the right side of Eq. (4) represent the interactions between Er^{3+} ion e_i in lattice E and Er^{3+} ion v_{gj} in lattice V_g , i.e., the interaction term considering the lattice edge and size effects.

Based on Eq. (4), the rate of the change of the population probability matrix $\mathbf{p}_k(E)$ at energy level k for all Er^{3+} ions in lattice E over time t is represented as

$$\begin{aligned} \frac{d\mathbf{p}_k(E)}{dt} = & - \sum_{k^*} (w_{a,kk^*} + w_{r,kk^*} + w_{nr,kk^*})\mathbf{p}_k(E) + \sum_{k^*} (w_{a,k^*k} + w_{r,k^*k} + w_{nr,k^*k})\mathbf{p}_{k^*}(E) \\ & - \sum_m \left[\sum_s (C_{km}^{(s)} \mathbf{D}_{E-E}^{(s)})\mathbf{p}_m(E) * \mathbf{p}_k(E) \right] + \sum_{k^*m^*} \left[\sum_s (C_{k^*m^*}^{(s)} \mathbf{D}_{E-E}^{(s)})\mathbf{p}_{m^*}(E) * \mathbf{p}_{k^*}(E) \right] \\ & - \sum_m \left\{ \sum_s \left[C_{km}^{(s)} \sum_g (\mathbf{D}_{E-V_g}^{(s)} \mathbf{p}_m(V_g)) \right] * \mathbf{p}_k(E) \right\} + \sum_{k^*m^*} \left\{ \sum_s \left[C_{k^*m^*}^{(s)} \sum_g (\mathbf{D}_{E-V_g}^{(s)} \mathbf{p}_{m^*}(V_g)) \right] * \mathbf{p}_{k^*}(E) \right\}, \quad (5) \end{aligned}$$

where $\mathbf{p}_m(V_g)$ is the population probability matrix for all Er^{3+} ions in lattice V_g at energy level m ; $\mathbf{D}_{E-E}^{(s)}$ is the distance coefficient matrix between Er^{3+} ions in lattice E , $\mathbf{D}_{E-E}^{(s)} = [d_{e_i, e_j}^{(s)}]$; and $\mathbf{D}_{E-V_g}^{(s)}$ is the distance coefficient matrix between Er^{3+} ions in lattice E and Er^{3+} ions in lattice V_g , $\mathbf{D}_{E-V_g}^{(s)} = [d_{e_i, v_{gj}}^{(s)}]$.

When distance $|\mathbf{M}_g|$ between lattice E and translational lattice V_g is greater than the lattice critical distance l_c (see Sec. C in the Supplemental Material [40] for the determination of l_c , $l_c = 50a$, a is the lattice constant of $\beta\text{-NaYF}_4$, $a = 5.969 \text{ \AA}$), the elements $d_{e_i, v_{gj}}^{(s)}$ in the matrix $\mathbf{D}_{E-V_g}^{(s)}$ can be considered equal to $|\mathbf{M}_g|^{-s}$. Meanwhile, the elements in the matrix $\mathbf{p}_m(V_g)$ can be replaced by the mean $\bar{P}_m(V_g)$ of all elements, $\bar{P}_m(V_g) = \sum_{i=1}^n P_m^{v_{gj}}/n$. Since lattice V_g is the same as lattice E (regardless of whether $|\mathbf{M}_g|$ is greater than l_c), $\mathbf{p}_m(V_g) = \mathbf{p}_m(E)$. Equation (5) is further rewritten as

$$\begin{aligned} \frac{d\mathbf{p}_k(E)}{dt} = & - \sum_{k^*} (w_{a,kk^*} + w_{r,kk^*} + w_{nr,kk^*})\mathbf{p}_k(E) + \sum_{k^*} (w_{a,k^*k} + w_{r,k^*k} + w_{nr,k^*k})\mathbf{p}_{k^*}(E) \\ & - \sum_m \left\{ \sum_s \left[C_{km}^{(s)} \left(\mathbf{D}_{E-E}^{(s)} + \sum_{|\mathbf{M}_g| \leq l_c} \mathbf{D}_{E-V_g}^{(s)} \right) \right] \mathbf{p}_m(E) * \mathbf{p}_k(E) \right\} - n \sum_m \left[\bar{P}_m(E) \mathbf{p}_k(E) \sum_s \left(C_{km}^{(s)} \sum_{|\mathbf{M}_g| > l_c} |\mathbf{M}_g|^{-s} \right) \right] \\ & + \sum_{k^*m^*} \left\{ \sum_s \left[C_{k^*m^*}^{(s)} \left(\mathbf{D}_{E-E}^{(s)} + \sum_{|\mathbf{M}_g| \leq l_c} \mathbf{D}_{E-V_g}^{(s)} \right) \right] \mathbf{p}_{m^*}(E) * \mathbf{p}_{k^*}(E) \right\} + n \sum_{k^*m^*} \left[\bar{P}_{m^*}(E) \mathbf{p}_{k^*}(E) \sum_s \left(C_{k^*m^*}^{(s)} \sum_{|\mathbf{M}_g| > l_c} |\mathbf{M}_g|^{-s} \right) \right], \quad (6) \end{aligned}$$

where n is the number of Er^{3+} ions in lattice E .

Equation (6) represents the final form of PMI. The complete and specific form of the equations in the $\beta\text{-NaYF}_4\text{:Er}^{3+}$ six-level system can be found in Sec. D in the Supplemental Material [40].

B. Periodic lattice modeling and calculation methods

1. Evaluation criterion for randomness of lattice modeling

To theoretically eliminate the influence of randomness of lattice modeling, the periodic translation of lattice E represents the microcrystalline particle U , which needs to meet two conditions: (i) the physical fields (i.e., the potential fields formed by the interaction between ions) where lattice E and translational lattice V_g are located are the same. (ii) the spatial distribution of Er^{3+} ions in lattice E is the same as that in translational lattice V_g . Because the size of particle U is much larger than that of lattice E , the position difference

between lattices E and V_g can be ignored, thus condition (i) holds.

Under the condition that the size of the microcrystalline particles and the doping concentration c_{Er} of Er^{3+} ion are known, the number $n_{U, \text{total}}$ of Y^{3+} and Er^{3+} ions in particle U and the number n_U of Er^{3+} ions in particle U are determined. After setting the scale of lattice geometric modeling, the numbers n_x , n_y , and n_z of unit cells contained in lattice E in the x , y , and z directions are determined. As a result, the number $n_{E, \text{total}}$ of Y^{3+} and Er^{3+} ions in lattice E is determined by $n_{E, \text{total}} = 1.5n_x n_y n_z$ (one $\beta\text{-NaYF}_4$ unit cell contains 1.5 Y^{3+} ions). Space Ω with the same shape and size as lattice E is randomly selected in particle U . In the doping process, Er^{3+} ions randomly replace Y^{3+} ions. Consequently, the number X of Er^{3+} ions in space Ω is a random variable following the hypergeometric distribution $X \sim H(n_{U, \text{total}}, n_U, n_{E, \text{total}})$. The doping concentration Z ($Z = X/n_{E, \text{total}}$) of Er^{3+} ions in space Ω is also a random variable.

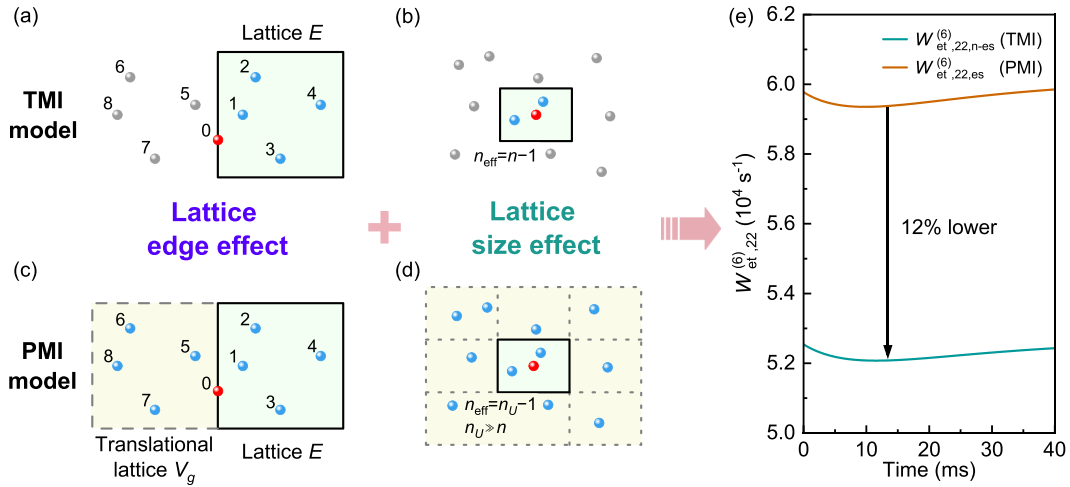


FIG. 2. Schematic diagram of the difference between the traditional microscopic rate equation model (TMI) and the periodic lattice microscopic rate equation model (PMI) proposed in this paper (see Sec. III). TMI only considers the interactions between Er^{3+} ions in lattice E , neglecting both the lattice edge and size effects. (a) In TMI, the interactions between the ion at the edge of lattice E (numbered 0) and ions outside lattice E (numbered 5, 6, 7, and 8) are neglected. (b) In TMI, the number n_{eff} of ions (blue) interacting with the investigated ion (red) is limited by the lattice modeling scale n , and $n_{\text{eff}} = n - 1$. By periodically translating the modeled lattice E , the PMI proposed in this paper (see Sec. III) considers not only the interactions between Er^{3+} ions in lattice E but also the interactions between Er^{3+} ions in lattice E and Er^{3+} ions in translational lattices V_g , correctly considering lattice edge and size effects. (c) In PMI, the interactions between the ion at the edge of lattice E (numbered 0) and ions outside lattice E (numbered 5, 6, 7, and 8) are considered. (d) In PMI, the number n_{eff} of ions (blue) interacting with the investigated ion (red) is not limited by the lattice modeling scale n , and $n_{\text{eff}} = n_U - 1$ (n_U is the number of Er^{3+} ions in the $\beta\text{-NaYF}_4\text{:Er}^{3+}$ microcrystalline particle, $n_U \gg n$). In the subgraphs (a)–(d), the interaction between the blue and red ions is considered, while the interaction between the gray and red ions is neglected. (e) The impact of neglecting lattice edge and size effects on the macroscopic energy-transfer rate. $W_{\text{et},22}^{(6)}$ and $W_{\text{et},22,\text{es}}^{(6)}$ represent the macroscopic energy-transfer rates neglecting and considering the lattice edge and size effects, respectively. Calculated under the conditions of 10% Er^{3+} ion doping concentration, excitation power density of 338.6 W/m^2 , and excitation time of 15 ms. The numbers n_x , n_y , and n_z of $\beta\text{-NaYF}_4$ unit cells in lattice E in the x , y , and z directions are 12, 12, and 10, respectively. The laser excitation occurs within the time interval of $-15 \text{ ms} \leq t \leq 0 \text{ ms}$ (not shown in the figure).

We use the relative standard deviation $\text{rsd}(Z)$ of Z as the criterion factor to quantify the randomness of lattice geometric

modeling. The criterion factor $\text{rsd}(Z)$ can be expressed as

$$\text{rsd}(Z) = \left[\frac{(n_{U,\text{total}} - n_U)(n_{U,\text{total}} - n_{E,\text{total}})}{n_{E,\text{total}} n_U (n_{U,\text{total}} - 1)} \right]^{1/2}. \quad (7)$$

As shown in Fig. 4(a), with the increase of the number $n_{E,\text{total}}$ of Y^{3+} and Er^{3+} ions in lattice E , the random fluctuation magnitude of Z decreases, and $\text{rsd}(Z)$ decreases.

What we need to pay attention to is the specific value of the criterion factor, so that the influence of lattice modeling randomness on microscopic model calculations can be ignored. Therefore, under different $\text{rsd}(Z)$ conditions of 18.07%, 5.72%, and 1.43%, the microscopic rate equations for multiple energy levels are solved, as shown in Figs. 4(b)–4(d). Namely, at each $\text{rsd}(Z)$ (i.e., the same $n_{E,\text{total}}$), lattice geometric modeling is randomly performed three times, and based on three sets of obtained spatial distributions of Er^{3+} ions, the microscopic rate equations are solved, respectively. When $\text{rsd}(Z)$ decreases from 18.07% to 1.43%, the luminescence decay curves of each energy level obtained from these three random lattice modeling schemes tend to be the same, reducing the randomness of lattice geometric modeling. It can be considered that, when $\text{rsd}(Z) < 1.5\%$ [Fig. 4(d)], the luminescence decay curves are very close to each other, indicating that the randomness of lattice geometric modeling on microscopic model calculations is very small and can be ignored. Therefore, this ensures that the doping concentration Z of Er^{3+} ions in space

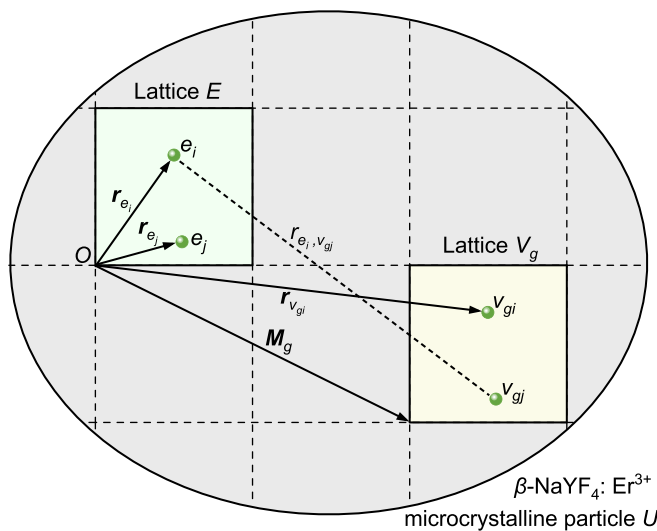


FIG. 3. The modeling process of the periodic lattice microscopic rate equation model. \mathbf{r}_{e_i} , \mathbf{r}_{e_j} and $\mathbf{r}_{v_{gi}}$ are coordinate vectors of ions e_i , e_j and v_{gi} , respectively. $r_{e_i,v_{gj}}$ is the distance between ion e_i and ion v_{gj} . \mathbf{M}_g is the vector from lattice E to lattice V_g .

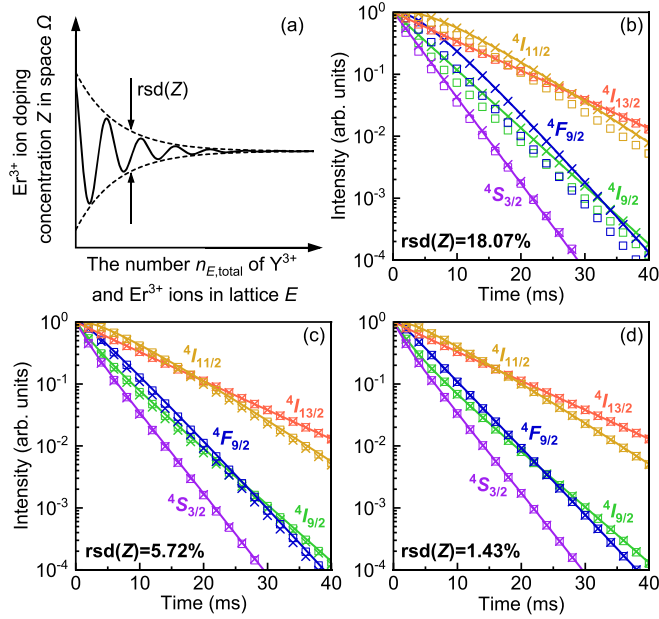


FIG. 4. (a) The curve of the doping concentration Z of Er^{3+} ions in space Ω vs the number $n_{E,\text{total}}$ of Y^{3+} and Er^{3+} ions in lattice E . The calculated luminescence decay curves of each energy level under different $\text{rsd}(Z)$: (b) $\text{rsd}(Z) = 18.07\%$, (c) $\text{rsd}(Z) = 5.72\%$, and (d) $\text{rsd}(Z) = 1.43\%$. The solid lines, squares, and crosses represent the luminescence decay curves obtained by lattice geometric modeling at the same scale and solving the microscopic rate equations for the first, second, and third times, respectively. The laser excitation occurs within the time interval of $-15 \text{ ms} \leq t \leq 0 \text{ ms}$ (not shown in the figure).

Ω is approximately constant, meeting the requirement of condition (ii).

In summary, the evaluation criterion of $\text{rsd}(Z) < 1.5\%$ is a sufficient criterion that meets the randomness requirement of lattice modeling. When this criterion is satisfied, the influence of lattice modeling randomness on equation model solving can be ignored.

2. Method for multiple modeling of periodic small-scale lattices

Based on the evaluation criterion for randomness of lattice modeling, we establish a multiple modeling method for periodic small-scale lattices in this section. This method reduces the computational complexity of the model while ensuring accuracy. In the particle U , f spaces Ω_i ($i = 1, 2, \dots, f$) with the same shape and size as lattice E are randomly selected. The number X_i and the doping concentration Z_i ($Z_i = X_i/n_{E,\text{total}}$) of Er^{3+} ions in Ω_i are random variables. The relative standard deviation $\text{rsd}(Z')$ of the average doping concentration Z' ($Z' = \sum_{i=1}^f Z_i/f$) of Er^{3+} ions in the spaces Ω_i ($i = 1, 2, \dots, f$) can be expressed as

$$\text{rsd}(Z') = \left[\frac{(n_{U,\text{total}} - n_U)(n_{U,\text{total}} - n_{E,\text{total}})}{f n_{E,\text{total}} n_U (n_{U,\text{total}} - 1)} \right]^{1/2}. \quad (8)$$

It is obvious that increasing f can reduce $n_{E,\text{total}}$ while keeping $\text{rsd}(Z')$ constant. As shown in Fig. 5(a), when the evaluation criterion of $\text{rsd}(Z') < 1.5\%$ is met, the computational time and the memory usage significantly decrease with

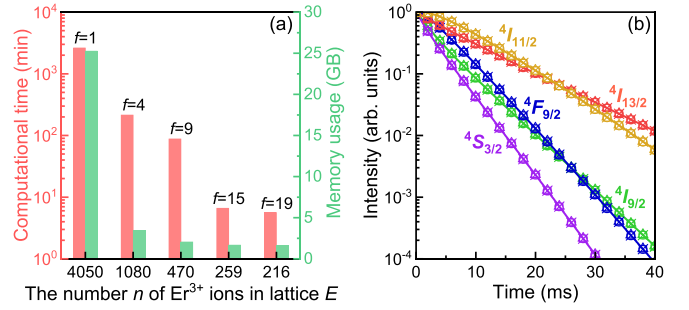


FIG. 5. (a) When $\text{rsd}(Z')$ is constant and $< 1.5\%$, the variation of computational time and memory usage with the number n of Er^{3+} ions in lattice E and the number f of modeling repetitions. (b) When $\text{rsd}(Z')$ is constant and $< 1.5\%$, the calculated luminescence decay curves under different n and f . The solid lines represent $n = 4050$ ($f = 1$), crosses $n = 1080$ ($f = 4$), squares $n = 470$ ($f = 9$), circles $n = 259$ ($f = 15$), and triangles $n = 216$ ($f = 19$). The laser excitation occurs within the time interval of $-15 \text{ ms} \leq t \leq 0 \text{ ms}$ (not shown in the figure). See Sec. E of Supplemental Material [40] for the calculation settings of subgraphs (a) and (b) and the reason multiple modeling of periodic small-scale lattices can reduce computational time.

the decrease of n ($n = n_{E,\text{total}} c_{\text{Er}}$, the known quantity c_{Er} is the doping concentration of Er^{3+} ion in the microcrystalline particles) and the increase of f . For example, when the condition changes from $n = 4050$ ($f = 1$) to $n = 216$ ($f = 19$), the computational time decreases by three orders of magnitude, from 2620.3 min to 5.6 min.

Based on the above analysis, we put forward a method for multiple modeling of periodic small-scale lattices instead of single modeling of large-scale lattices. The implementation steps of the method are as follows. **Step 1:** Lattice geometric modeling is performed to obtain lattice E . **Step 2:** Using the spatial distribution information of Er^{3+} ions in lattice E , the microscopic rate equations for periodic lattices are solved, and the average population probability $\bar{P}_{k,i}(E)$ of Er^{3+} ions in lattice E at energy level k is obtained (subscript i represents the calculation result obtained from the i th repetition of **Steps 1** and **2**). **Step 3:** Repeat **Steps 1** and **2** f times to obtain $\bar{P}_{k,i}(E)$ ($i = 1, 2, \dots, f$). The average value $\sum_{i=1}^f \bar{P}_{k,i}(E)/f$ is the final solution of the microscopic rate equations for periodic lattices.

When the evaluation criterion of $\text{rsd}(Z') < 1.5\%$ is met (i.e., satisfying the randomness requirement of lattice modeling), we conduct these steps at different values of n and f , and the results are shown in Fig. 5(b). Under different combinations of n and f , the calculation results are approximately the same, indicating the rationality of using multiple modeling of periodic small-scale lattices instead of single modeling of large-scale lattices.

It is worth noting that, as the lattice modeling scale n decreases, the spatial distribution of Er^{3+} ions in the modeled microcrystalline particle U (U is composed of lattice E and translational lattices V_g) becomes more regular, and the dynamics of more Er^{3+} ions are artificially synchronized, which does not occur in reality. Therefore, to avoid artifacts in computations, n cannot be arbitrarily small. In Fig. S4 in the Supplemental Material [40], we determine that the lower

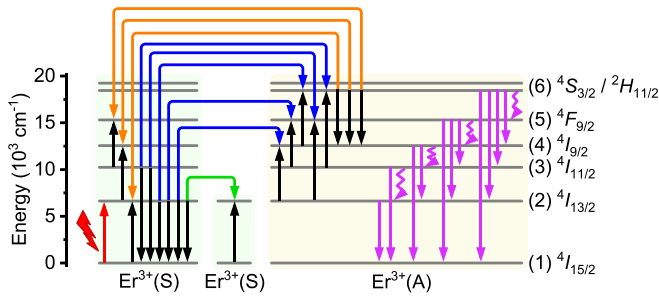


FIG. 6. Energy-level diagram of β -NaYF₄:Er³⁺ six-level system under 1510 nm laser excitation. The spectral term symbols and the index numbers of energy levels in the rate equations are shown on the right side of the figure. The red arrow represents the stimulated absorption process. The purple straight-line and polyline arrows represent the radiative relaxation processes and the multiphonon relaxation processes, respectively. The energy transfer processes include energy migration (EM; green arrow) between sensitizers (S), energy transfer (ET; blue arrows) from a sensitizer to an activator (A), and cross-relaxation (CR; orange arrows) from an activator to a sensitizer.

limit of n is 100. That is, when $n \geq 100$, multiple modeling of small-scale lattices of size n can replace single modeling of large-scale lattices.

3. Steps to determine the scale of lattice geometric modeling

To reduce the computational time while ensuring model accuracy, we adopt the following steps to determine the scale of lattice geometric modeling (see Sec. E in the Supplemental Material [40] for the scale we adopted):

Step 1: Given the size of the microcrystalline particles and the doping concentration c_{Er} of Er³⁺ ion, the number $n_{U,\text{total}}$ of Y³⁺ and Er³⁺ ions in particle U and the number n_U of Er³⁺ ions in particle U are determined.

Step 2: Based on the computational capability of the computer, we choose the value of the number n of Er³⁺ ions in lattice E (n is no less than 100 and is generally taken as 150–500). According to the formula $n_{E,\text{total}} = n/c_{\text{Er}}$, the number $n_{E,\text{total}}$ of Y³⁺ and Er³⁺ ions in lattice E is determined.

Step 3: According to Eq. (8), we calculate the minimum value of the number f of modeling repetitions that meet the evaluation criterion of $\text{rsd}(Z') < 1.5\%$.

Step 4: By using the formula $n_{E,\text{total}} = 1.5n_x n_y n_z$ (one β -NaYF₄ unit cell contains 1.5 Y³⁺ ions), the numbers n_x , n_y , and n_z of β -NaYF₄ unit cells in lattice E in the x , y , and z directions are determined.

IV. DETERMINATION OF ENERGY TRANSFER MICROPARAMETERS

As illustrated in Fig. 6, considering the stimulated absorption process, radiative relaxation processes, multiphonon relaxation processes, and energy transfer processes of Er³⁺ ions in the β -NaYF₄:Er³⁺ UCL system, we get the specific

form of PMI in this system (see Sec. D in the Supplemental Material [40]). Taking the β -NaYF₄:Er³⁺ six-level system as an example, we introduce how to determine the microscopic intrinsic parameters of energy transfer through the inverse problem analysis of PMI.

The forward problem of the microscopic model is solved to obtain the population probability of Er³⁺ ions at various energy levels (see Sec. F in the Supplemental Material [40]). Then by using the spatial statistical average of population probability, the macroscopic luminescence phenomenon of the upconversion system can be predicted and characterized. From the perspective of the forward problem of the model, the macroscopic luminescence characteristics of the β -NaYF₄:Er³⁺ six-level upconversion system depend on the following 35 intrinsic parameters: 1 stimulated absorption rate $w_{a,12}$, 11 radiative relaxation rates w_{r,kk^*} , 4 multiphonon relaxation rates w_{nr,kk^*} , and 19 energy transfer microparameters $C_{km}^{(s)}$. In our previous work [41,42], the absorption cross-section and intrinsic relaxation rates of Er³⁺ ions have been obtained, such as $w_{a,12}$, w_{r,kk^*} , and w_{nr,kk^*} . The energy transfer microparameters cannot be determined through the inverse problem analysis of the macroscopic rate equation model. Moreover, due to the limitations of TMI in terms of accuracy and computational time, it has become very difficult to accurately determine the inter-ion energy transfer microparameters.

However, PMI established in this paper not only improves the model accuracy but also significantly reduces the computational complexity, making the inverse problem calculation of large-scale ion groups at multiple energy levels feasible. Therefore, the inverse problem of PMI can be solved to obtain $C_{km}^{(s)}$ (see Sec. G in the Supplemental Material [40]). For the β -NaYF₄:Er³⁺ six-level system, there are 19 unknown energy transfer microparameters $C_{km}^{(s)}$ in the equation. To overcome the ill-posedness of inverse problem solving, it is necessary to utilize multiple sets of mutually independent experimental data under different doping concentrations and energy levels. We prepared β -NaYF₄:Er³⁺ microcrystalline particle samples (#B-0, #B-1, and #B-2) with Er³⁺ ion doping concentrations of 1%, 2%, and 10% by high-temperature solid-state method (see Sec. H in the Supplemental Material [40]). The luminescence decay curves of five energy levels (⁴I_{13/2}, ⁴I_{11/2}, ⁴I_{9/2}, ⁴F_{9/2}, and ⁴S_{3/2}) for three samples were measured (Fig. 7) using a 1510 nm laser with a repetition rate of 10 Hz and a duty cycle of 15% as the excitation source.

A global fitting procedure (particle swarm optimization) is used to solve the inverse problem of the microscopic rate equation model using all experimental data simultaneously (15 luminescence decay curves at three different doping concentrations and five energy levels). To simultaneously fit multiple energy transfer microparameters and ensure the search efficiency of the particle swarm optimization, we set the population size to 350. The algorithm requires ~ 300 iterations, i.e., 105 000 forward problem calculations, to obtain the optimal fitting results. Under the setting conditions of our lattice geometric modeling (see Sec. E in the Supplemental Material [40]), it takes ~ 5 min to solve the forward problem of PMI. Therefore, if parallel computation is performed using a 100-core CPU, solving the inverse problem of this model will

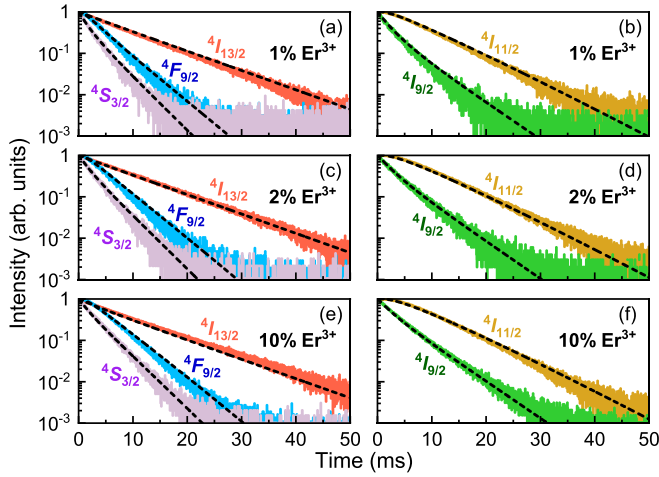


FIG. 7. The measured and fitted luminescence decay curves for each energy level. (a) and (b) Sample #B-0, excitation power density of 768.0 W/m²; (c) and (d) sample #B-1, excitation power density of 567.4 W/m²; and (e) and (f) sample #B-2, excitation power density of 338.6 W/m². The solid and dashed lines represent the measured and fitted results, respectively. The laser excitation occurs within the time interval of $-15 \text{ ms} \leq t \leq 0 \text{ ms}$ (not shown in the figure).

take ~ 3.64 d. However, if we use the same CPU to calculate TMI, solving the forward problem of this traditional model once will take at least 1000 min, while solving the inverse problem of this model will require at least 729 d. Therefore, it is obvious that our model demonstrates significant advantages,

greatly reducing computational time and making it possible to determine the energy transfer microparameters through the inverse problem analysis.

The experimental data and the fitting results of the luminescence decay curves are shown in Fig. 7, which is in good agreement. For samples #B-0, #B-1, and #B-2, the reduced residual sum of squares for energy levels $^4I_{13/2}$, $^4I_{11/2}$, $^4I_{9/2}$, $^4F_{9/2}$, and $^4S_{3/2}$ reach the order of 10^{-4} to 10^{-5} . Based on the fitting results, we experimentally obtain the energy transfer microparameters $C_{km}^{(s)}$ and provide the calculation uncertainty of the results ranging from 2.0% to 21.2%, as shown in Table I (see Sec. I in the Supplemental Material [40] for analysis of calculation uncertainties). This is a comprehensive report on the measurement data of intrinsic parameters of inter-ion energy transfer for multilevel nonlinear UCL systems.

In addition, we used Kushida's [43] method to calculate the theoretical values of the energy transfer microparameters. Due to the limitations of the theoretical approach, there exists a significant deviation between the theoretical values and our measured values. This is also the reason we cannot directly use the theoretical values of energy transfer microparameters in applications. Therefore, this is the significance of this paper, which lies in the use of PMI to achieve a highly precise determination of the microscopic intrinsic parameters of energy transfer.

V. CONCLUSIONS

In summary, we developed PMI for upconversion dynamics and determination of the microparameters of energy

TABLE I. Theoretical values, measured values, and calculation uncertainties of inter-ion energy transfer microparameters. Theoretical values are calculated by Kushida's [43] method considering the transition selection rules [44].

Parameter	Theoretical value based on Kushida's [43] method (cm ³ s ⁻¹)	Measured value using our model (cm ³ s ⁻¹)	Calculation uncertainty
$C_{21}^{(6)}$	17.6×10^{-40}	0.010×10^{-40}	15.1%
$C_{22}^{(6)}$	9.47×10^{-40}	2.403×10^{-40}	4.0%
$C_{23}^{(6)}$	21.9×10^{-40}	13.530×10^{-40}	8.8%
$C_{24}^{(6)}$	5.35×10^{-40}	14.030×10^{-40}	5.8%
$C_{32}^{(6)}$	0.765×10^{-40}	34.273×10^{-40}	2.0%
$C_{33}^{(6)}$	0.423×10^{-40}	4.519×10^{-40}	13.0%
$C_{61}^{(6)}$	11.7×10^{-40}	38.127×10^{-40}	2.9%
$C_{62}^{(6)}$	6.29×10^{-40}	27.650×10^{-40}	2.6%
$C_{63}^{(6)}$	14.5×10^{-40}	31.924×10^{-40}	9.0%
$C_{21}^{(8)}$	3.95×10^{-54}	0.010×10^{-54}	20.1%
$C_{22}^{(8)}$	1.1×10^{-54}	8.262×10^{-54}	15.1%
$C_{23}^{(8)}$	2.45×10^{-54}	16.395×10^{-54}	12.4%
$C_{24}^{(8)}$	0.599×10^{-54}	18.088×10^{-54}	2.2%
$C_{32}^{(8)}$	0.41×10^{-54}	21.392×10^{-54}	7.7%
$C_{33}^{(8)}$	0.227×10^{-54}	0	—
$C_{61}^{(8)}$	1.31×10^{-54}	4.695×10^{-54}	4.6%
$C_{62}^{(8)}$	0.0231×10^{-54}	10.486×10^{-54}	8.8%
$C_{21}^{(10)}$	4.13×10^{-69}	0.010×10^{-69}	4.4%
$C_{22}^{(10)}$	0.0726×10^{-69}	5.076×10^{-69}	21.2%

transfer between ions, achieving the correlation between micro-ion interactions and macroluminescence. TMI neglects the lattice edge and size effects, leading to an underestimation of $\sim 12\%$ in the macroscopic energy-transfer rate. We proposed a processing method for ionic interactions in periodic lattices, greatly improving the accuracy of the microscopic model. Furthermore, we proposed an evaluation criterion of $\text{rsd}(Z') < 1.5\%$ for randomness of lattice modeling. By quantitatively assessing the randomness of lattice geometric modeling, we established a multiple modeling method for periodic small-scale lattices, replacing single modeling of large-scale lattices. This eliminates the influence of randomness of lattice geometric modeling on microscopic model calculations, significantly reducing the computational complexity of the model (computational time is reduced by three orders of magnitude) while ensuring accuracy. To solve the inverse problem of PMI, we measured 15 luminescence decay curves at three different doping concentrations and five energy levels. By incorporating the particle swarm

optimization, we obtained 19 energy transfer microparameters between Er^{3+} ions in the $\beta\text{-NaYF}_4\text{:Er}^{3+}$ six-level system and provided the calculation uncertainty of the results ranging from 2.0% to 21.2%. This paper is of great significance for revealing the mechanisms of UCL, providing important theoretical models and measurement data for regulating and optimizing the luminescence performance of the upconversion system. By utilizing our model and the energy transfer microparameters, a precise targeted design of the upconversion system can be achieved, meeting the requirements of high quantum yield, long persistence, and deep tissue penetration, especially in the field of bio-imaging and photodynamic therapy.

ACKNOWLEDGMENTS

This paper was supported by the National Natural Science Foundation of China (Grant No. 51976097) and the National Science and Technology Major Project (No. J2019-V-0006-0099).

-
- [1] F. Auzel, Upconversion and anti-Stokes processes with f and d ions in solids, *Chem. Rev.* **104**, 139 (2004).
- [2] J. Zhao, D. Jin, E. P. Schartner, Y. Lu, Y. Liu, A. V. Zvyagin, L. Zhang, J. M. Dawes, P. Xi, J. A. Piper *et al.*, Single-nanocrystal sensitivity achieved by enhanced upconversion luminescence, *Nat. Nanotechnol.* **8**, 729 (2013).
- [3] F. Liu, Y. Liang, and Z. Pan, Detection of up-converted persistent luminescence in the near infrared emitted by the $\text{Zn}_3\text{Ga}_2\text{GeO}_8\text{:Cr}^{3+}$, Yb^{3+} , Er^{3+} phosphor, *Phys. Rev. Lett.* **113**, 177401 (2014).
- [4] F. T. Rabouw, P. T. Prins, P. Villanueva-Delgado, M. Castelijns, R. G. Geitenbeek, and A. Meijerink, Quenching pathways in $\text{NaYF}_4\text{:Er}^{3+}$, Yb^{3+} upconversion nanocrystals, *ACS Nano* **12**, 4812 (2018).
- [5] H. Liu, C. T. Xu, G. Dumlupinar, O. B. Jensen, P. E. Andersen, and S. Andersson-Engels, Deep tissue optical imaging of upconverting nanoparticles enabled by exploiting higher intrinsic quantum yield through use of millisecond single pulse excitation with high peak power, *Nanoscale* **5**, 10034 (2013).
- [6] F. Pini, L. Francés-Soriano, V. Andriago, M. M. Natile, and N. Hildebrandt, Optimizing upconversion nanoparticles for FRET biosensing, *ACS Nano* **17**, 4971 (2023).
- [7] L. Liang, D. B. L. Teh, N.-D. Dinh, W. Chen, Q. Chen, Y. Wu, S. Chowdhury, A. Yamanaka, T. C. Sum, C.-H. Chen *et al.*, Upconversion amplification through dielectric superlensing modulation, *Nat. Commun.* **10**, 1391 (2019).
- [8] Q.-X. Wang, Y.-F. Yang, X.-F. Yang, Y. Pan, L.-D. Sun, W.-Y. Zhang, Y. Shao, J. Shen, J. Lin, L. Li *et al.*, Up-converted/downshifted NaLnF_4 and metal-organic framework heterostructures boosting NIR-II imaging-guided photodynamic immunotherapy toward tumors, *Nano Today* **43**, 101439 (2022).
- [9] S. Bhuckory, S. Lahtinen, N. Höysniemi, J. Guo, X. Qiu, T. Soukka, and N. Hildebrandt, Understanding FRET in upconversion nanoparticle nucleic acid biosensors, *Nano Lett.* **23**, 2253 (2023).
- [10] A. Hlaváček, Z. Farka, M. J. Mickert, U. Kostiv, J. C. Brandmeier, D. Horák, P. Skládal, F. Foret, and H. H. Gorris, Bioconjugates of photon-upconversion nanoparticles for cancer biomarker detection and imaging, *Nat. Protoc.* **17**, 1028 (2022).
- [11] A. M. Kaczmarek, M. Suta, H. Rijckaert, A. Abalymov, I. Van Driessche, A. G. Skirtach, A. Meijerink, and P. Van Der Voort, Visible and NIR upconverting Er^{3+} – Yb^{3+} luminescent nanorattles and other hybrid PMO-inorganic structures for *in vivo* nanothermometry, *Adv. Funct. Mater.* **30**, 2003101 (2020).
- [12] C. Lee, E. Z. Xu, K. W. C. Kwock, A. Teitelboim, Y. Liu, H. S. Park, B. Ursprung, M. E. Ziffer, Y. Karube, N. Fardian-Melamed *et al.*, Indefinite and bidirectional near-infrared nanocrystal photoswitching, *Nature (London)* **618**, 951 (2023).
- [13] J. Zuo, D. Sun, L. Tu, Y. Wu, Y. Cao, B. Xue, Y. Zhang, Y. Chang, X. Liu, X. Kong *et al.*, Precisely tailoring upconversion dynamics via energy migration in core-shell nanostructures, *Angew. Chem. Int. Ed.* **130**, 3108 (2018).
- [14] H. Liu, K. Huang, R. R. Valiev, Q. Zhan, Y. Zhang, and H. Ågren, Photon upconversion kinetic nanosystems and their optical response: Photon upconversion kinetic nanosystems and their optical response, *Laser Photonics Rev.* **12**, 1700144 (2018).
- [15] N. P. Hylton, T. F. Hinrichsen, A. R. Vaquero-Stainer, M. Yoshida, A. Pusch, M. Hopkinson, O. Hess, C. C. Phillips, and N. J. Ekins-Daukes, Photoluminescence upconversion at GaAs/InGaP₂ interfaces driven by a sequential two-photon absorption mechanism, *Phys. Rev. B* **93**, 235303 (2016).
- [16] J. Liao, M. Wang, F. Lin, Z. Han, B. Fu, D. Tu, X. Chen, B. Qiu, and H.-R. Wen, Thermally boosted upconversion and downshifting luminescence in $\text{Sc}_2(\text{MoO}_4)_3\text{:Yb/Er}$ with two-dimensional negative thermal expansion, *Nat. Commun.* **13**, 2090 (2022).
- [17] R. Martín-Rodríguez, R. Valiente, F. Rodríguez, F. Piccinelli, A. Speghini, and M. Bettinelli, Temperature dependence and temporal dynamics of Mn^{2+} upconversion luminescence sensitized by Yb^{3+} in codoped $\text{LaMgAl}_{11}\text{O}_{19}$, *Phys. Rev. B* **82**, 075117 (2010).

- [18] Y. Liu, Y. Lu, X. Yang, X. Zheng, S. Wen, F. Wang, X. Vidal, J. Zhao, D. Liu, Z. Zhou *et al.*, Amplified stimulated emission in upconversion nanoparticles for super-resolution nanoscopy, *Nature (London)* **543**, 229 (2017).
- [19] W. Ren, G. Lin, C. Clarke, J. Zhou, and D. Jin, Optical nanomaterials and enabling technologies for high-security-level anticounterfeiting, *Adv. Mater.* **32**, 1901430 (2020).
- [20] B. Zhou, L. Yan, J. Huang, X. Liu, L. Tao, and Q. Zhang, NIR II-responsive photon upconversion through energy migration in an ytterbium sublattice, *Nat. Photonics* **14**, 760 (2020).
- [21] Y. Xie, Y. Song, G. Sun, P. Hu, A. Bednarkiewicz, and L. Sun, Lanthanide-doped heterostructured nanocomposites toward advanced optical anti-counterfeiting and information storage, *Light Sci. Appl.* **11**, 150 (2022).
- [22] Y. Zhuang, D. Chen, W. Chen, W. Zhang, X. Su, R. Deng, Z. An, H. Chen, and R.-J. Xie, X-ray-charged bright persistent luminescence in $\text{NaYF}_4:\text{Ln}^{3+}@\text{NaYF}_4$ nanoparticles for multidimensional optical information storage, *Light Sci. Appl.* **10**, 132 (2021).
- [23] N. J. J. Johnson, S. He, S. Diao, E. M. Chan, H. Dai, and A. Almutairi, Direct evidence for coupled surface and concentration quenching dynamics in lanthanide-doped nanocrystals, *J. Am. Chem. Soc.* **139**, 3275 (2017).
- [24] Q. Zhan, H. Liu, B. Wang, Q. Wu, R. Pu, C. Zhou, B. Huang, X. Peng, H. Ågren, and S. He, Achieving high-efficiency emission depletion nanoscopy by employing cross relaxation in upconversion nanoparticles, *Nat. Commun.* **8**, 1058 (2017).
- [25] J. Ganem, J. Crawford, P. Schmidt, N. W. Jenkins, and S. R. Bowman, Thulium cross-relaxation in a low phonon energy crystalline host, *Phys. Rev. B* **66**, 245101 (2002).
- [26] W. J. C. Grant, Role of rate equations in the theory of luminescent energy transfer, *Phys. Rev. B* **4**, 648 (1971).
- [27] F. Pini, L. Francés-Soriano, N. Peruffo, A. Barbon, N. Hildebrandt, and M. M. Natile, Spatial and temporal resolution of luminescence quenching in small upconversion nanocrystals, *ACS Appl. Mater. Interfaces* **14**, 11883 (2022).
- [28] P. Loiko and M. Pollnau, Stochastic model of energy-transfer processes among rare-earth ions. Example of $\text{Al}_2\text{O}_3:\text{Tm}^{3+}$, *J. Phys. Chem. C* **120**, 26480 (2016).
- [29] L. Agazzi, K. Wörhoff, and M. Pollnau, Energy-transfer-upconversion models, their applicability and breakdown in the presence of spectroscopically distinct ion classes: A case study in amorphous $\text{Al}_2\text{O}_3:\text{Er}^{3+}$, *J. Phys. Chem. C* **117**, 6759 (2013).
- [30] M. Inokuti and F. Hirayama, Influence of energy transfer by the exchange mechanism on donor luminescence, *J. Chem. Phys.* **43**, 1978 (1965).
- [31] M. Yokota and O. Tanimoto, Effects of diffusion on energy transfer by resonance, *J. Phys. Soc. Jpn.* **22**, 779 (1967).
- [32] I. R. Martin, V. D. Rodriguez, U. R. Rodriguez-Mendoza, V. Lavin, E. Montoya, and D. Jaque, Energy transfer with migration. Generalization of the Yokota-Tanimoto model for any kind of multipole interaction, *J. Chem. Phys.* **111**, 1191 (1999).
- [33] L. D. Zusman, Kinetics of luminescence damping in the hopping mechanism of quenching, *Sov. Phys. JETP* **46**, 347 (1977).
- [34] D. F. de Sousa, R. Lebullenger, A. C. Hernandez, and L. A. O. Nunes, Evidence of higher-order mechanisms than dipole-dipole interaction in $\text{Tm}^{3+} \rightarrow \text{Tm}^{3+}$ energy transfer in fluoroindogallate glasses, *Phys. Rev. B* **65**, 094204 (2002).
- [35] P. Villanueva-Delgado, K. W. Krämer, R. Valiente, M. De Jong, and A. Meijerink, Modeling blue to UV upconversion in $\beta\text{-NaYF}_4:\text{Tm}^{3+}$, *Phys. Chem. Chem. Phys.* **18**, 27396 (2016).
- [36] P. Villanueva-Delgado, K. W. Krämer, and R. Valiente, Simulating energy transfer and upconversion in $\beta\text{-NaYF}_4:\text{Yb}^{3+}, \text{Tm}^{3+}$, *J. Phys. Chem. C* **119**, 23648 (2015).
- [37] B. Grauel, C. Würth, C. Homann, L. Krukewitt, E. Andresen, J. Roik, S. Recknagel, M. Haase, and U. Resch-Genger, Volume and surface effects on two-photon and three-photon processes in dry co-doped upconversion nanocrystals, *Nano Res.* **15**, 2362 (2022).
- [38] J. L. Philipsen and A. Bjarklev, Monte Carlo simulations of homogeneous upconversion in erbium-doped silica glasses, *IEEE J. Quantum Electron.* **33**, 845 (1997).
- [39] S. Spelthann, J. Thiem, O. Melchert, R. Komban, C. Gimmler, A. Demicran, A. Ruehl, and D. Ristau, Predicting the excitation dynamics in lanthanide nanoparticles, *Adv. Opt. Mater.* **11**, 2300096 (2023).
- [40] See Supplemental Material at <http://link.aps.org/supplemental/10.1103/PhysRevB.110.045105> for details of lattice geometric modeling, the specific form of the microscopic rate equation model, the methods for solving the forward and inverse problems, and the analysis of calculation uncertainties.
- [41] L. Fu, Y. Wu, C. Zhang, T. Fu, and C. Shi, Determination of radiative and multiphonon non-radiative relaxation rates of upconversion materials, *Phys. Chem. Chem. Phys.* **24**, 9953 (2022).
- [42] L. Fu, Y. Wu, and T. Fu, Determination of absorption cross-section of RE^{3+} in upconversion powder materials: Application to $\beta\text{-NaYF}_4:\text{Er}^{3+}$, *J. Lumin.* **245**, 118758 (2022).
- [43] T. Kushida, Energy transfer and cooperative optical transitions in rare-earth doped inorganic materials. I. transition probability calculation, *J. Phys. Soc. Jpn.* **34**, 1318 (1973).
- [44] P. A. Tanner and C.-K. Duan, Luminescent lanthanide complexes: Selection rules and design, *Coord. Chem. Rev.* **254**, 3026 (2010).